Full paper

Achieving high-precision laparoscopic manipulation through adaptive force control

ALEXANDRE KRUPA [1,*], GUILLAUME MOREL [2]
and MICHEL DE MATHELIN [1]

[1] *University of Strasbourg I, LSIIT (UMR CNRS 7005), ENSPS, Bd S. Brant, 67400 Illkirch, France*
[2] *University of Paris 6, LRP6 (CNRS FRE2705), 18, route du Panorama, BP61,
92265 Fontenay aux Roses Cedex, France*

Abstract—In this paper, we present a new solution to laparoscopic manipulation based on force-feedback control. This method allows us to both explicitly control the forces applied to the patient through the trocar and to precisely control the position of the surgical instrument. It does not require any geometrical model of the operative environment nor any fine robot base placement prior to the instrument insertion. Different adaptive control strategies involving different kinds of sensory equipments are proposed. These strategies are experimentally validated on a laboratory apparatus. An experiment is also presented where a laparoscope held by the robot's arm tracks a target through visual servoing.

Keywords: Medical robotics; laparoscopic manipulation; force control; visual servoing.

1. INTRODUCTION

Over the past decade, laparoscopic surgery has been the object of important research activity in the robotics community. In this application, the robot system has to manipulate a surgical instrument introduced inside the patient's abdomen through a trocar placed at an incision point. Usually, this trocar is kinematically modeled as a 2-translational-d.o.f. constraint. Thus, the manipulation can be formulated as a 4-d.o.f. problem. Two different kinds of robotic systems have been developed and are now available for clinical use.

One system is the Intuitive Surgical da Vinci system that exploits a 4-d.o.f. robotic device, exhibiting a fixed remote center of rotation placed at the trocar 'center' [1, 2] (see Fig. 1a). Such a system suffers from several limitations. First, prior to the

---

*To whom correspondence should be addressed. E-mail: alexandre.krupa@ensps.u-strasbg.fr or krupa@eavr.u-strasbg.fr
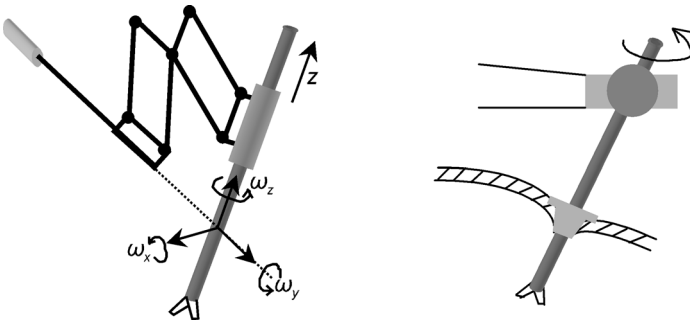
Figure 1. (a) Remote center of rotation. (b) Passive wrist.

insertion of the instrument, the robot base has to be finely placed so that the remote center of rotation precisely fits with the trocar center. Also, an additional 6-d.o.f. mechanism is required for the robot base placement, which drastically increases the overall system complexity. In the environment of a surgical room, this may involve a fastidious process. Note that this process may have to be run several times in the same surgical operation. Indeed, in a complex surgical procedure, several trocars are placed in the patient's abdomen and the surgeon needs to use different entry points during the operation, which requires the robot base to be moved. Finally, there is no way of limiting the forces applied to the patient: in the case of a displacement of the trocar, due to motion of the patient, the forces applied to the trocar may increase without any control.

The second strategy for laparoscopic manipulation, proposed by Computer Motion Inc. in the Zeus system, consists of using a 6-d.o.f. device, only four of them being actuated [3]. The 2 free d.o.f. are placed in the robot wrist, so that the instrument naturally rotates around the trocar when the wrist center is moved at a given location by the three first joints of the robot (see Fig. 1b). This allows us to significantly simplify the robot placement process prior to the operation. Indeed, the robot can be placed independently from the trocar locations in the patient abdomen. The robot can also access, from the same base placement, several entry points. Furthermore, a displacement of the trocar due to possible motion of the patient does not produce any forces on the trocar. However, this system also suffers from practical limitations, due to the fact that the 2-d.o.f. constraint is only rough approximation of the kinematics of the trocar–instrument link. For example, the robot often has to manipulate a thin instrument (e.g. 5 mm diameter) through a relatively large trocar (e.g. 15–20 mm). Indeed, the choice of the trocar diameter is global for the whole operation and corresponds to the largest instrument that has to be used in the corresponding entry point. Thus, backlash may appear between the instrument and the trocar. Combined with the free d.o.f. of the robot, this may lead to uncontrolled motions of the instrument and a lack of precision for the surgeon that complicates the manipulation. Furthermore, when the instrument exerts forces to the organs, a balancing force is applied by the instrument to the trocar, which is not desirable.
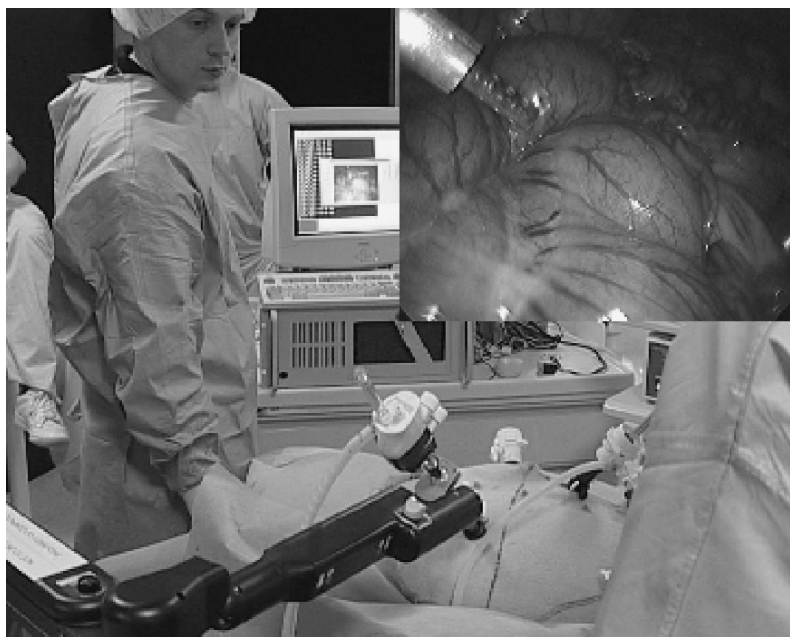
Figure 2. Live experiments of automatic vision-based control for laparoscopic surgery using the Zeus system.

   This problem is crucial in research that we are developing in cooperation with IRCAD (Institut de Recherche sur le Cancer de l'Apprareil Digestif, Strasbourg, France) of Professor Marescaux. In this research (*cf.*, Ref. [4]), visual servoing is used to control the motion of the instrument from the laparoscope image (see Fig. 2). With such an automatic control of the surgical gesture, in some configurations, the backlash between the instrument and the trocar may lead to a cyclic oscillation of the controller.

   We propose in Ref. [5] a different approach to laparoscopic manipulation that overcomes the above-mentioned limitations. The manipulator possesses six actuated joints, providing 6 operational d.o.f. for the instrument. In order to cope with the trocar constraint, a force sensor is placed at the end-effector of the robot. A force controller is then used to explicitly control the lateral forces applied to the trocar towards zero. Different control strategies are proposed. Since there is no *a priori* knowledge of the trocar location with respect to the base, these strategies involve an adaptive estimation of the distance from the end-effector to the trocar center. The paper is organized as follows. Section 2 details the kinematic modeling of laparoscopic manipulation. Section 3 formulates the basic force control loop that is implemented to limit the forces applied to the patient and gives experimental results. Sections 4 and 5 propose two different strategies to identify on-line the distance from the robot to the trocar, in order to improve the efficiency of the proposed method. They are both theoretically demonstrated and experimentally validated on a laboratory apparatus. Finally, the last section describes a visual servoing application

where a laparoscope held by the robot automatically tracks a a surgical instrument by controlling the 4 d.o.f. with a hybrid force/vision controller.

2. MODELING

We consider a 6-d.o.f. robot, equipped with a force sensor and handling a rigid laparoscopic instrument, introduced in a patient's abdomen through a trocar. The kinematics of the laparoscopic manipulation is depicted in Fig. 3, where $\mathcal{F}_t = \{O_t, \mathbf{x}_t, \mathbf{y}_t, \mathbf{z}_t\}$ is the tool frame attached to the tip of the instrument, such that the $\mathbf{z}_t$ axis is colinear to the instrument penetration axis; $\mathcal{F}_s = \{O_s, \mathbf{x}_s, \mathbf{y}_s, \mathbf{z}_s\}$ is the F/T sensor frame, with $\mathbf{z}_s$ colinear to $\mathbf{z}_t$; P is the point of the instrument handler that instantaneously coincides with the trocar; l is the fixed distance between the origins of $\mathcal{F}_s$ and $\mathcal{F}_t$; and d is the variable distance from P to the origin of $\mathcal{F}_t$. For the sake of simplicity, without loss of generality, it is assumed that the axes of $\mathcal{F}_s$ are aligned with the axes of $\mathcal{F}_t$, i.e. $\mathbf{x}_t = \mathbf{x}_s$ and $\mathbf{y}_t = \mathbf{y}_s$.

The trocar is modeled as a planar kinematic constraint, given by:

$$\mathbf{v}_p^\mathrm{T}\mathbf{x}_t = \mathbf{v}_p^\mathrm{T}\mathbf{y}_t = 0, \tag{1}$$

where $\mathbf{v}_p$ denotes the velocity of point P, considering the motion of the instrument relatively to the patient. In the sequel, the patient is supposed to be fixed with respect to the robot base. In order to parameterize the instantaneous velocity of the instrument with respect to the patient, which is supposed to be fixed, we use the following four-component operational space vector:

$$\mathbf{w} = (\dot{d} \quad \omega_x \quad \omega_y \quad \omega_z)^\mathrm{T}, \tag{2}$$

where $\dot{d} = \mathbf{v}_p^\mathrm{T}\mathbf{z}_t$ is the instrument penetration velocity, along $\mathbf{z}_t$, and ω_x, ω_y and ω_z are projections of the absolute rotational velocity $\boldsymbol{\omega}$ over $\mathbf{x}_t$, $\mathbf{y}_t$ and $\mathbf{z}_t$, respectively.

Combining (1) and (2), one gets:

$$\begin{pmatrix} {}^t\mathbf{v}_p \\ {}^t\boldsymbol{\omega} \end{pmatrix} = \begin{pmatrix} \mathbf{0}_{2\times4} \\ \mathbf{I}_{4\times4} \end{pmatrix} \mathbf{w}, \tag{3}$$
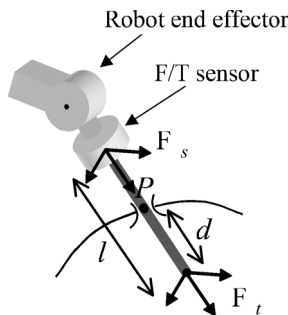

Figure 3. Manipulation through a trocar.

where the upper-left superscript t indicates that the vector is expressed in the frame $\mathcal{F}_t$, $\mathbf{0}_{2\times4}$ is a 2-by-4 zero matrix and $\mathbf{I}_{4\times4}$ is the 4-by-4 identity matrix. Furthermore, the absolute velocity of the instrument at its tip O_t is given by:

$$\begin{pmatrix} {}^t\mathbf{v}_{O_t} \\ {}^t\boldsymbol{\omega} \end{pmatrix} = \mathbf{M}(d) \begin{pmatrix} {}^t\mathbf{v}_p \\ {}^t\boldsymbol{\omega} \end{pmatrix}, \tag{4}$$

$$\text{with} \quad \mathbf{M}(d) = \begin{pmatrix} \mathbf{I}_{3\times3} & \begin{pmatrix} 0 & d & 0 \\ -d & 0 & 0 \\ 0 & 0 & 0 \end{pmatrix} \\ \mathbf{0}_{3\times3} & \mathbf{I}_{3\times3} \end{pmatrix}. \tag{5}$$

Conventional robot kinematic modeling can then be used to provide the jacobian matrix $\mathbf{J}(q)$ mapping the joint velocity $\dot{q}$ into the instrument tip velocity $({}^t\mathbf{v}_{O_t}^T \ {}^t\boldsymbol{\omega}^T)^T$:

$$\begin{pmatrix} {}^t\mathbf{v}_{O_t}^T \\ {}^t\boldsymbol{\omega}^T \end{pmatrix} = \mathbf{J}(q)\dot{q}. \tag{6}$$

We finally get the inverse kinematic model:

$$\dot{q} = \mathbf{J}^{-1}(q)\mathbf{M}(d) \begin{pmatrix} \mathbf{0}_{2\times4} \\ \mathbf{I}_{4\times4} \end{pmatrix} \mathbf{w}, \tag{7}$$

where it is assumed that the robot kinematics is non-singular.

Equation (7) shows that the knowledge of the scalar parameter d is sufficient to provide a robot motion that satisfies the trocar constraint (1). However, in practice, this parameter is not precisely known. Applying (7) with an estimated depth $\widehat{d} \neq d$ will provide a lateral motion at the trocar center, thus generating forces. To cope with this problem, force control can be used.

3. FORCE-FEEDBACK CONTROL

3.1. Control design

Let $\mathbf{f}$ be the force applied by the instrument to the patient through the trocar. We assume here that the lateral force at the instrument tip can be neglected, like, for example, in camera positioning or surgical applications that mainly require forces along the instrument direction. Thus, the force $\mathbf{f}$ is directly sensed at the force sensor. The two components of $\mathbf{f}$ along $\mathbf{x}_s = \mathbf{x}_t$ and $\mathbf{y}_s = \mathbf{y}_t$ are $\mathbf{f}_x$ and $\mathbf{f}_y$, respectively. The aim of the force feedback loop is to servo them towards zero. Considering a motion rate control strategy, a simple proportional controller can be used:

$$\begin{cases} \mathbf{x}_t^{Tt}\mathbf{v}_p^* = -k\mathbf{f}_x \\ \mathbf{y}_t^{Tt}\mathbf{v}_p^* = -k\mathbf{f}_y, \end{cases} \tag{8}$$

where ${}^t\mathbf{v}_p^*$ is the control input velocity of point P expressed in $\mathcal{F}_t$. We can now use a hybrid position/force control strategy, that is to control simultaneously the motion

w along the 4 free d.o.f. and the forces $\mathbf{f}_x$ and $\mathbf{f}_y$ along the 2 constrained d.o.f. This is achieved by the following control law:

$$\dot{q}^* = \mathbf{J}^{-1}(q)\mathbf{M}(\widehat{d})\left[\begin{pmatrix} \mathbf{0}_{2\times4} \\ \mathbf{I}_{4\times4} \end{pmatrix} \mathbf{w}^* - k \begin{pmatrix} \mathbf{I}_{2\times2} \\ \mathbf{0}_{4\times2} \end{pmatrix} \begin{pmatrix} \mathbf{f}_x \\ \mathbf{f}_y \end{pmatrix}\right] = \mathbf{J}^{-1}(q)\mathbf{M}(\widehat{d}) \begin{pmatrix} -k\mathbf{f}_x \\ -k\mathbf{f}_y \\ \mathbf{w}^* \end{pmatrix},$$

(9)

where $\dot{q}^*$ is the joint velocity control input, $\widehat{d}$ is the estimate of d and $\mathbf{w}^*$ is the input velocity for the instrument motion. Note that $\mathbf{w}^*$ is usually directly set by the surgeon through the teleoperation interface, but it can also be controlled autonomously, from a vision feedback loop, as illustrated in Section 6. In the sequel, $\mathbf{w}^*$ is supposed to be arbitrary. Also, we will assume, hereafter, that the velocity-controlled robot has a large bandwidth as compared to the external force loop so that:

$$\dot{q} \simeq \dot{q}^*.$$

(10)

It can be seen in (9) that the distance d has to be estimated in order to implement the control law. Again, this distance is not precisely identified, which can limit the practical efficiency of the force control feedback loop.

3.2. Experimental results

Experiments where performed on a laboratory apparatus, consisting of a 6-d.o.f. robot, equipped with a force sensor and manipulating a rigid 0.3-m length surgical
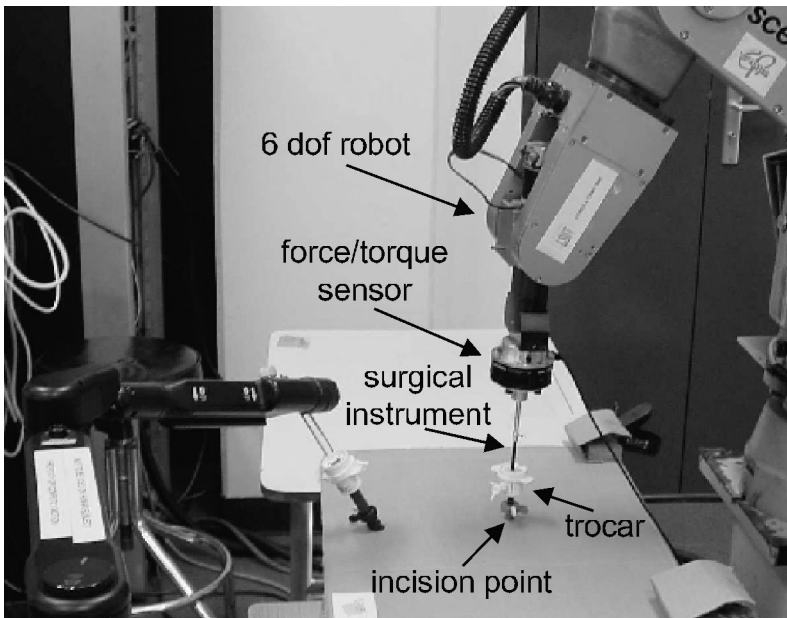

Figure 4. Laboratory experimental setup.

instrument through a trocar placed at a surgical endoscopic training device (see
Fig. 4). A PC (600 Mhz) is used to acquire the forces and control the robot
at a sampling rate of 50 Hz. For these experiments, the velocity input $\mathbf{w}^*$ is set
to $(0, \omega_x^*, \omega_y^*, 0)$. The two rotational components are 0.05 Hz, ± 1.5 deg/s square
signals. The objective is to evaluate the influence on the estimation error $\widehat{d} - d$
on the closed loop force control performance. Figure 5 shows the forces $\mathbf{f}_x$ and $\mathbf{f}_y$
measured for different values of $\widehat{d}$ and d. In the first configuration, $\widehat{d} = 0.15$ m
and $d = 0.2$ m. The maximum forces obtained are $|\mathbf{f}_x| \simeq 2$ N and $|\mathbf{f}_y| \simeq 2$ N.
In the second configuration, $\widehat{d} = 0.3$ m and $d = 0.1$ m, the maximum forces are
$|\mathbf{f}_x| \simeq 4$ N and $|\mathbf{f}_y| \simeq 5$ N. Finally, in the third configuration, $\widehat{d} = 0.02$ m and
$d = 0.2$, the maximum forces are $|\mathbf{f}_x| \simeq 5$ N and $|\mathbf{f}_y| \simeq 4$ N. Clearly, forces
increase with the estimation error on d due to the unknown distance d in the control
law. These forces are due to the fact that a low gain k has to be used for the force
control, so as to guarantee stable and robust behavior of the force loop. In surgical
conditions, force larger than 5 N applied to the patient's abdomen is too high and
may tear the abdominal wall around the incision point. Increasing k would reduce
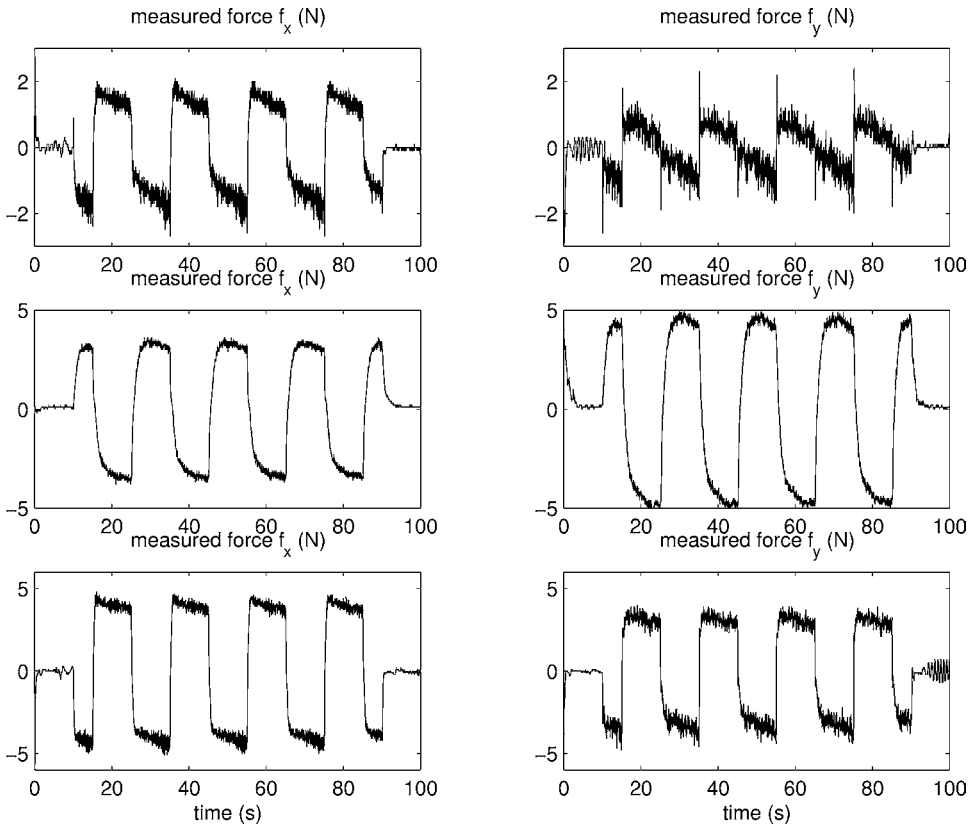

Figure 5. Forces $\mathbf{f}_x$ and $\mathbf{f}_y$ for different values of $\widehat{d}$. First row: $\widehat{d} = 0.15$ m and $d = 0.2$ m. Second
row: $\widehat{d} = 0.3$ m and $d = 0.1$ m. Third row: $\widehat{d} = 0.02$ m and $d = 0.2$ m.

the forces, but may cause chattering in some configurations. Thus, it is desirable to provide a way to estimate on-line the penetration depth $\widehat{d}$, in order to obtain a higher performance of the force loop. Two strategies are developed in the Sections 4 and 5.

4. DEPTH ESTIMATION WITH FORCE SENSING ONLY

4.1. Adaptive control design

In the first strategy, we consider that the force sensing device only provides a measurement for $\mathbf{f}_x$ and $\mathbf{f}_y$. We then have to reconsider the ideal model given by constraint (1). A residual lateral displacement of point P is introduced:

$$\mathbf{v}_p^T \mathbf{x}_t = \dot{x}_p, \quad \mathbf{v}_p^T \mathbf{y}_t = \dot{y}_p. \tag{11}$$

This lateral displacement generates a force. A simplified model of the interaction between the robot and the patient at the incision point is used (e.g. like, in Refs [6, 7]):

$$\mathbf{f}_x = g.x_p, \quad \mathbf{f}_y = g.y_p, \tag{12}$$

where g is the stiffness constant of the patient's abdominal wall. Applying the control law (9), and combining with equations (4)–(6) and (10)–(12), one gets the following closed loop behavior:

$$\begin{cases} \dot{\mathbf{f}}_x = g^t \mathbf{v}_p^T \mathbf{x}_t = g\left(-k\mathbf{f}_x + (\widehat{d} - d)\omega_y^*\right) \\ \dot{\mathbf{f}}_y = g^t \mathbf{v}_p^T \mathbf{y}_t = g\left(-k\mathbf{f}_y - (\widehat{d} - d)\omega_x^*\right) \end{cases}. \tag{13}$$

These equations are linear with respect to the parameterization error $(d - \widehat{d})$.

Assuming that g is known, we propose the following normalized gradient algorithm to estimate d:

$$\dot{\widehat{d}} = \dot{d}^* - k_1\left(\dot{\mathbf{f}}_x + gk\mathbf{f}_x\right)\frac{\omega_y^*}{\epsilon + \omega_x^{*2} + \omega_y^{*2}} + k_1\left(\dot{\mathbf{f}}_y + gk\mathbf{f}_y\right)\frac{\omega_x^*}{\epsilon + \omega_x^{*2} + \omega_y^{*2}} \tag{14}$$

where $k_1 > 0$ is the gain of the gradient algorithm and $\epsilon > 0$ is a normalization coefficient. In order to cope with the speed of change of the distance d during the intervention, $\dot{d}^*$ is added in the estimation law to integrate the control velocity along the instrument axis $\mathbf{z}_t$. The stability and convergence properties of this estimation algorithm are given in the following Lemma.

LEMMA 1. *Stability and convergence properties of the estimation algorithm* (14)
1. *The estimated parameter $\widehat{d}$ and its derivative are bounded, i.e. $\widehat{d}, \dot{\widehat{d}} \in L_\infty$.*

2. *The error signal $e = \sqrt{\dfrac{\omega_x^{*2} + \omega_y^{*2}}{\epsilon + \omega_x^{*2} + \omega_y^{*2}}} e_p \in L_2 \cap L_\infty$*

3. *The parameter estimation error, $e_p = (d - \widehat{d})$, converges, i.e. $\lim_{t\to\infty} e_p = e_{p\infty}$.*

4. If $\sqrt{\dfrac{\omega_x^{*2} + \omega_y^{*2}}{\epsilon + \omega_x^{*2} + \omega_y^{*2}}}$ is persistently exciting, i.e.

$$\exists \eta > 0 \; \exists T \text{ s.t. } \frac{1}{T} \int_{t_0}^{t_0+T} \frac{\omega_x^{*2} + \omega_y^{*2}}{\epsilon + \omega_x^{*2} + \omega_y^{*2}} \, dt > \eta > 0, \quad \forall t_0 \geqslant 0, \tag{15}$$

then, $\lim_{t \to \infty} e_p = 0$, *exponentially.*

The proof of this Lemma is given in the Appendix. We can see that the algorithm is stable and that the convergence of the parameter error to zero is obtained if there is enough excitation (i.e. rotational motions around axis $\mathbf{x}_t$ and $\mathbf{y}_t$). Note that, since $0 < d < l$, a projection is added to always keep the estimate $\widehat{d}$ in the interval $[0, l]$:

$$
\begin{aligned}
\dot{\widehat{d}} &= 0 \quad \text{if } \widehat{d} = 0 \text{ and } \dot{\widehat{d}} < 0, \\
\dot{\widehat{d}} &= 0 \quad \text{if } \widehat{d} = l \text{ and } \dot{\widehat{d}} > 0.
\end{aligned}
\tag{16}
$$

In practice, the stiffness parameter may not be known. In this case, noticing that (13) is linear with respect to the stiffness coefficient g, we propose the following gradient algorithm to estimate on-line both parameters g and d:

$$
\begin{aligned}
\dot{\widehat{d}} &= \dot{d}^* - k_1 \left(\dot{\mathbf{f}}_x + \widehat{g} k \mathbf{f}_x \right) \frac{\omega_y^*}{\epsilon + \omega_x^{*2} + \omega_y^{*2}} + k_1 \left(\dot{\mathbf{f}}_y + \widehat{g} k \mathbf{f}_y \right) \frac{\omega_x^*}{\epsilon + \omega_x^{*2} + \omega_y^{*2}}, \\
\dot{\widehat{g}} &= -k_1 \left(\dot{\mathbf{f}}_x + \widehat{g} k \mathbf{f}_x \right) k \mathbf{f}_x - k_1 \left(\dot{\mathbf{f}}_y + \widehat{g} k \mathbf{f}_y \right) k \mathbf{f}_y,
\end{aligned}
\tag{17}
$$

where $k_1 > 0$ is the gain of this gradient algorithm and $\epsilon > 0$ is a normalization coefficient. The stability and convergence properties of this estimation algorithm are given in the following Lemma.

LEMMA 2. *Stability and convergence properties of the estimation algorithm* (17)
1. $\widehat{d}, \widehat{g} \in L_\infty$ and $\dot{\widehat{d}}, \dot{\widehat{g}} \in L_\infty$.
2. *If* $\mathbf{Q}^{1/2}$ *is persistently exciting, then* $\lim_{t \to \infty} e_p = 0$, *exponentially, where*

$$
\mathbf{Q} = \begin{pmatrix} \dfrac{g^2}{\rho^2} \left(\omega_x^{*2} + \omega_y^{*2} \right) & \dfrac{gk}{\rho^2} \left(\mathbf{f}_x \omega_y^* - \mathbf{f}_y \omega_x^* \right) \\ gk \left(\mathbf{f}_x \omega_y^* - \mathbf{f}_y \omega_x^* \right) & k^2 \left(\mathbf{f}_x^2 + \mathbf{f}_y^2 \right) \end{pmatrix} \geqslant 0
$$

with $\rho(t) = \sqrt{\epsilon + \omega_x^{*2}(t) + \omega_y^{*2}(t)}$.

The proof of this Lemma is given in the Appendix. We can see that the parameter convergence to zero is obtained if there are rotational motions around $\mathbf{x}_t$ and $\mathbf{y}_t$ as well as translational motions along $\mathbf{x}_t$ and $\mathbf{y}_t$.

4.2. Experimental results

Experiments where conducted on the same laboratory apparatus. The first experiment intends to provide an identification of g using (17). This parameter is identified

on the experimental setup by applying excited force reference signals f_x^*, f_y^* shown in Fig. 6. For this stiffness identification experiment, the value of $\hat{d}$ was set constant to the real distance $d = 0.15$ m. The identified stiffness is shown in Fig. 7 and converges to the value $\hat{g} = 2580$ N/m. It can be seen that the convergence is rather robust and stable, in spite of the noise in the force signal. For the force-feedback control, using the same initial conditions as in experiments of Section 3.2, but now aplying the algorithm (14) with the constant identified parameter $\hat{g} = 2580$ N/m to on-line estimate d, we obtained the experimental results plotted in Fig. 8. The convergence of $\hat{d}$ from its initial value d_0 to the true value d is shown experimentally with an accuracy of about 7 mm. The error in the estimation of d is mainly due to the backlash between the instrument and the incision point. Together with the convergence of d, one can see that the forces applied to the patient are limited to 2 N in spite of the small error in the estimation of d. This value of 2 N is a reasonable force applied on the abdominal wall. Although the measured force suffers from significant noise, the estimation is smooth. This is due to the low bandwidth of the estimation dynamics that rejects the high-frequency noise in $\mathbf{f}$ and $\dot{\mathbf{f}}$, thanks
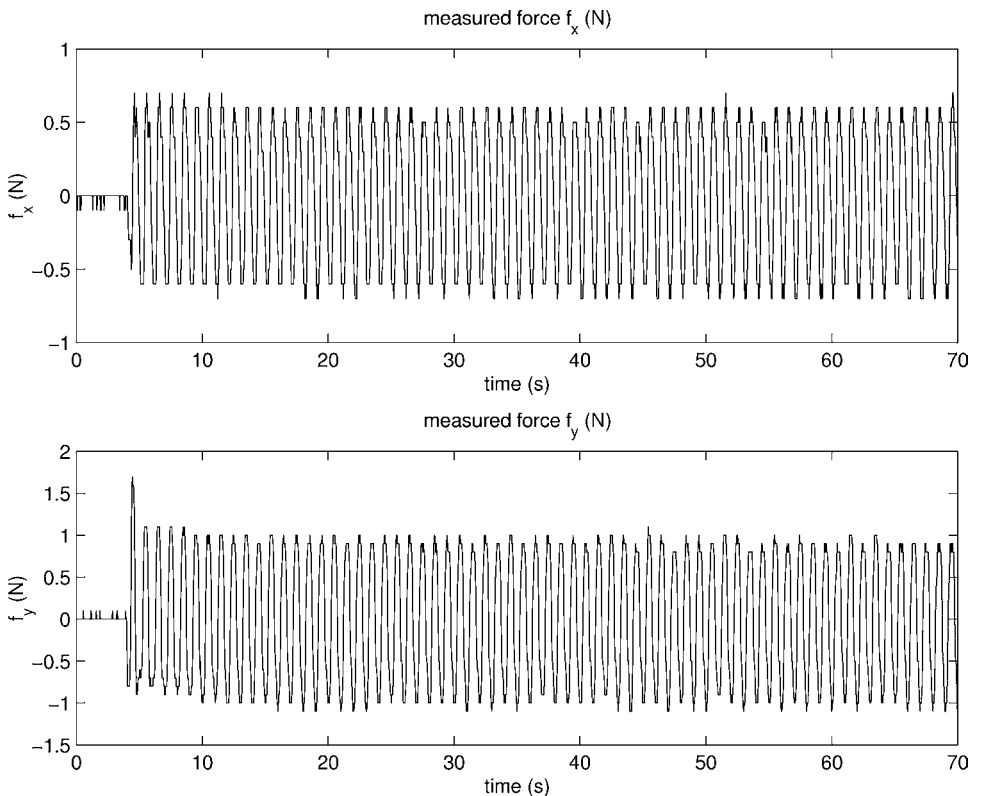

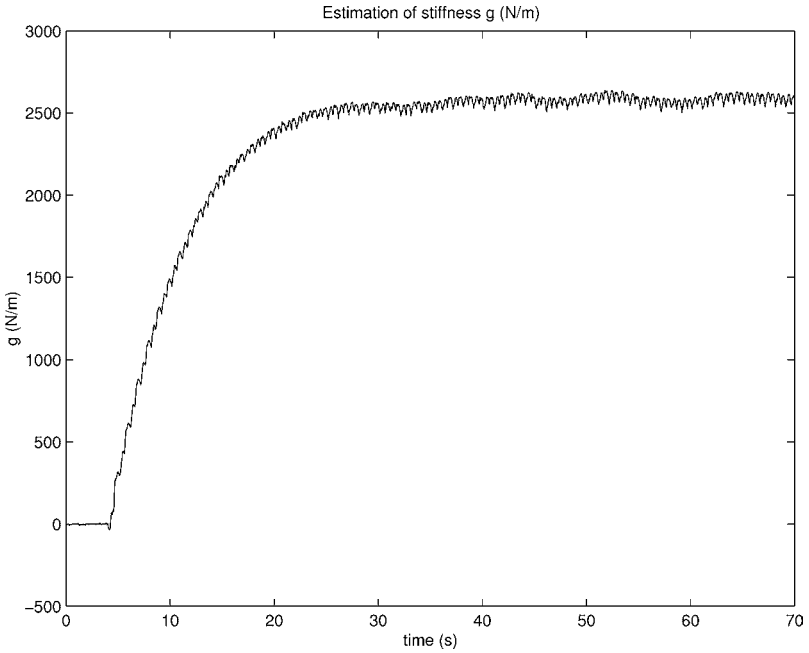**Figure 6.** Forces applied to identify the stiffness parameter g.

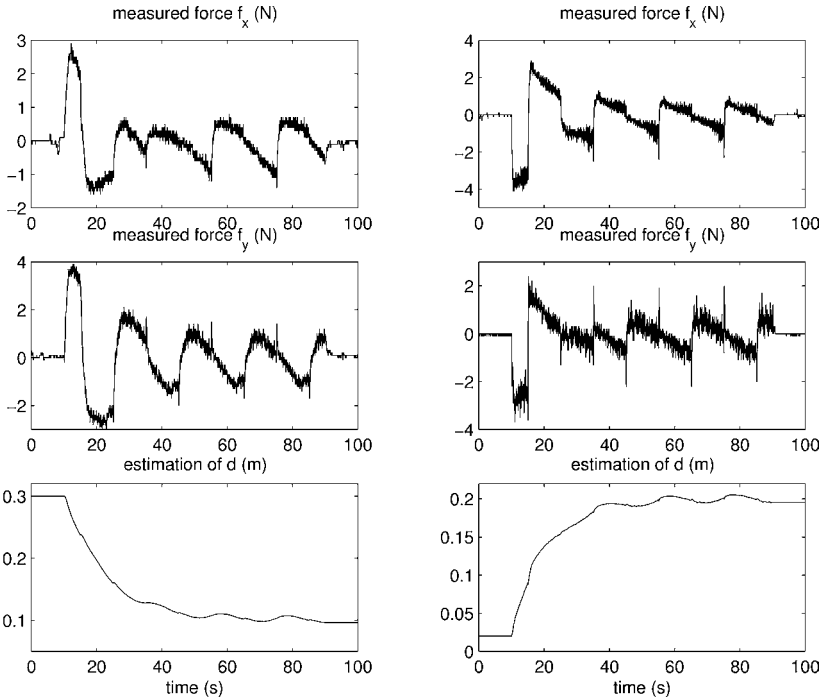**Figure 7.** Identified stiffness $\hat{g}$ (experimental result).

Figure 8. Adaptive estimation of d (experimental results). Left column: $d_0 = 0.3$ and $d = 0.1$ m. Right column: $d_0 = 0.02$ m and $d = 0.2$ m.

to the use of a low gain k_1. As a price, the convergence is slower. The next section proposes an alternative strategy for a faster identification of d.

5. ROBUST IDENTIFICATION OF THE DISTANCE d FROM FORCE AND TORQUE MEASUREMENTS

5.1. Depth estimation algorithm

In this section, we assume that the six-component interaction wrench can be completely measured by the force/torque sensor. In this case, the distance, d, can be identified from the measurements of the forces $\mathbf{f}_x$, $\mathbf{f}_y$ and the torques $\boldsymbol{\gamma}_x$, $\boldsymbol{\gamma}_y$. Indeed, we have:

$$m = l - d = \frac{\sqrt{\boldsymbol{\gamma}_x^2 + \boldsymbol{\gamma}_y^2}}{\sqrt{\mathbf{f}_x^2 + \mathbf{f}_y^2}} \triangleq \frac{\boldsymbol{\gamma}_\mathrm{r}}{\mathbf{f}_\mathrm{r}}. \tag{18}$$

However, (18) cannot be used directly to estimate d. Indeed, when the force control algorithm brings the force closed to zero, the estimation can become inaccurate due to the noise and resolution of the sensor. Therefore, we propose to use a weighted least-squares algorithm with a sliding window and a dead-zone to robustly estimate m and d (*cf.*, Ref. [8]).

To minimize the estimation error, let us define the following cost function with a sliding window and forgetting factor:

$$J(t, t_0) = \int_{\max(t-T, t_0)}^{t} \mathrm{e}^{-\lambda(t-\tau)} \left[\boldsymbol{\gamma}_\mathrm{r}(\tau) - \mathbf{f}_\mathrm{r}(\tau) \widehat{m}(t) \right]^2 \mathrm{d}\tau, \tag{19}$$

where $\lambda > 0$ is a forgetting factor and $T > 0$ is the size of the sliding window. Then, the least-squares estimate $\widehat{m}(t)$ that minimizes $J(t, t_0)$ is equal to:

$$\widehat{m}(t) = R(t, t_0)^{-1} Q(t, t_0), \tag{20}$$

with:

$$R(t, t_0) = \int_{\max(t-T, t_0)}^{t} \mathrm{e}^{-\lambda(t-\tau)} \mathbf{f}_\mathrm{r}^2(\tau) \, \mathrm{d}\tau, \tag{21}$$

$$Q(t, t_0) = \int_{\max(t-T, t_0)}^{t} \mathrm{e}^{-\lambda(t-\tau)} \mathbf{f}_\mathrm{r}(\tau) \boldsymbol{\gamma}_\mathrm{r}(\tau) \, \mathrm{d}\tau. \tag{22}$$

In practice, the estimate is not reliable when $\mathbf{f}_\mathrm{r}$ or $\boldsymbol{\gamma}_\mathrm{r}$ is closed to zero. Therefore, if $\mathbf{f}_\mathrm{r}(t)$ or $\boldsymbol{\gamma}_\mathrm{r}(t)$ decreases below some threshold value $\mathbf{f}_\mathrm{th}$ or $\boldsymbol{\gamma}_\mathrm{th}$, the computation of the least-squares estimate is frozen, i.e. only the reference instrument velocity $\dot{d}^*$ along the $\mathbf{z}_\mathrm{t}$ axis is taken into account in order to cope with the change of d due to the control velocity. The least-squares estimate is computed only if the forces and

torques are larger than the threshold values for a minimum length of time $T_0 \leqslant T$. Consequently, the robust estimation algorithm is defined as follows:

$$\widehat{d}(t) = \begin{cases} l - R(t, t_k)^{-1} Q(t, t_k) & \text{if } \mathbf{f}_r(t) > \mathbf{f}_{\text{th}} \text{ and } \boldsymbol{\gamma}_r(t) > \boldsymbol{\gamma}_{\text{th}} \text{ and } t \geqslant t_k + T_0 \\ \widehat{d}(T_k) + \int_{T_k}^t \dot{d}*(\tau) \, d\tau & \text{otherwise,} \end{cases}$$

(23)

where t_k is the last time instant when $\mathbf{f}_r$ and $\boldsymbol{\gamma}_r$ left the dead-zone area, and T_k is the last time instant when $\mathbf{f}_r$ or $\boldsymbol{\gamma}_r$ entered the dead-zone area, i.e.:

$$(\mathbf{f}_r(t_k) = \mathbf{f}_{\text{th}} \text{ or } \boldsymbol{\gamma}_r(t_k) = \boldsymbol{\gamma}_{\text{th}}) \quad \text{and } (\mathbf{f}_r(t_k^+) > \mathbf{f}_{\text{th}} \text{ and } \boldsymbol{\gamma}_r(t_k^+) > \boldsymbol{\gamma}_{\text{th}})$$

$$(\mathbf{f}_r(T_k) = \mathbf{f}_{\text{th}} \text{ or } \boldsymbol{\gamma}_r(T_k) = \boldsymbol{\gamma}_{\text{th}}) \quad \text{and } (\mathbf{f}_r(T_k^+) < \mathbf{f}_{\text{th}} \text{ or } \boldsymbol{\gamma}_r(T_k^+) < \boldsymbol{\gamma}_{\text{th}}), \quad (24)$$

Furthermore, since $0 < d < l$, a saturation function is applied on the estimate, so that it always stays in the interval $[0, l]$.

5.2. Experimental results

Figure 9 presents the experimental result for the direct estimation of d using the robust estimation algorithm. The experimental results are obtained with maximum size $T = 0.5$ s of the sliding window and the minimum size $T_0 = 0.25$ s. In order
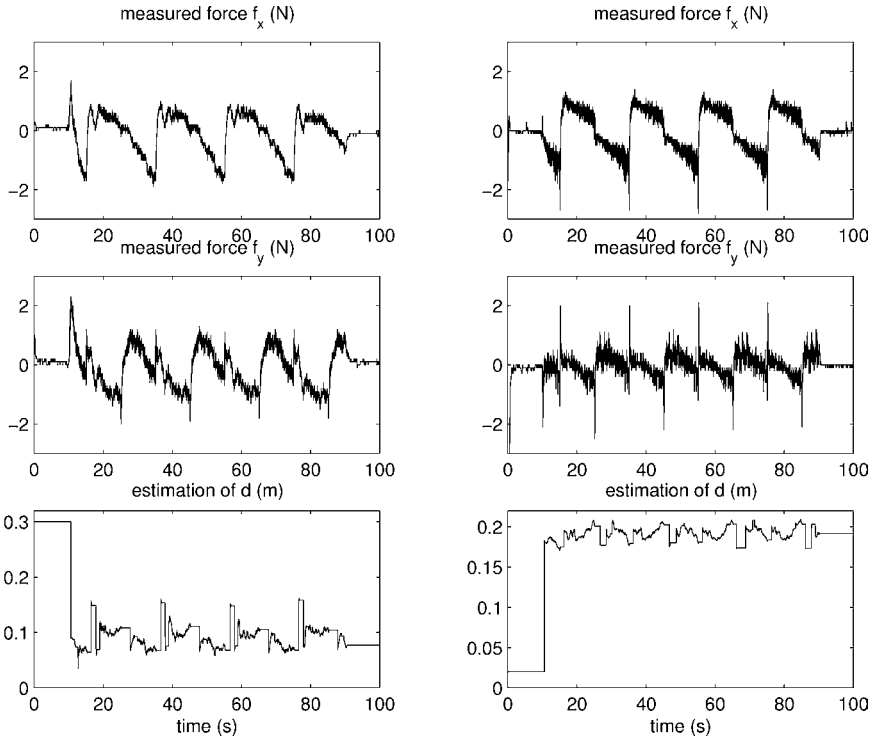

Figure 9. Direct estimation of d (experimental results). Left column: $d_0 = 0.3$ m and $d = 0.1$ m. Right column: $d_0 = 0.02$ m and $d = 0.2$ m.

to compare these results with the previous ones, the experimental conditions for d_0 and d are reproduced. We can see that with the least-squares estimator the estimated signal $\widehat{d}$ exhibits larger noise than the gradient algorithm estimator of Section 4. For $d = 10$ cm the maximum error is 5 cm, whereas for $d = 20$ cm the maximum error is reduced to 2 cm. This difference is due to the change of the signal/noise ratio of the measured torque which is proportional to the distance d. However, the convergence of the estimation algorithm is faster, as it does not involve any dynamics. The noise on $\widehat{d}$ does not significantly affect the force response, since the force applied to the abdominal wall is also below the reasonable value of 2 N, as compared to Fig. 8.

6. HYBRID VISUAL AND FORCE CONTROL

Other experiments have been realized with the 6-d.o.f. robot system using visual servoing technics. A laparoscopic camera is held instead of the surgical instrument and the image from this camera is used to move the robot to accomplish a specific task like, e.g. to track another surgical instrument in the work space (see Fig. 10). This type of experiment has been already realized with a 4-d.o.f. structure [9–11]. However, to our knowledge, such a combination of force and visual feedback has never been realized in a laparoscopic application. We will assume, hereafter, that the tool frame attached to the tip of the instrument $\mathcal{F}_t$ is also the laparoscopic camera frame of reference. We realize an experiment where the laparoscope tracks another surgical instrument. The head of the instrument to be tracked is identified as a segment of known length σ_0. From the image processing, we extract the following features: the image coordinates (u,v) of the center of the segment in the image, the image length σ of the segment which provides depth information (if σ_0 is known) and the angle φ of the segment with respect to the $\mathbf{x}_t$ axis of $\mathcal{F}_t$. All this features are presented in Fig. 11. Therefore the visual feature vector $\mathbf{s}$ is defined as:
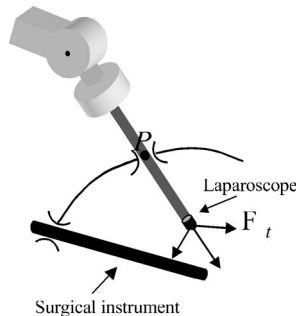

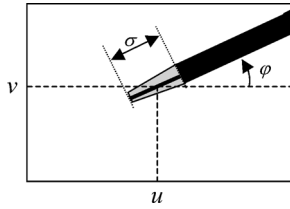**Figure 10.** Tracking of surgical instrument by the laparoscope.

Figure 11. Visual features used for the instrument-tracking task.

$$\mathbf{s} = \begin{pmatrix} u \\ v \\ \sigma \\ \varphi \end{pmatrix}. \tag{25}$$

For visual servoing, we use the classical image-based control strategy (*cf.*, Ref. [12]). Therefore, the reference velocity of the laparoscope $\mathbf{w}^*$ is chosen proportional to the error on the feature:

$$\mathbf{w}^* = \mathbf{k_s}\mathbf{J_I}(\mathbf{s}^* - \mathbf{s}), \tag{26}$$

where $\mathbf{k_s}$ is a positive scalar and $\mathbf{s}^* = [u^*v^*\sigma^*\varphi^*]^T$ is the reference trajectory of the visual features in the image. $\mathbf{J_I}$ is an approximation of the interaction matrix relating $\mathbf{w}$ to $\dot{\mathbf{s}}$. To simplify the interaction matrix, we use the assumption that the optical axis is orthogonal to the instrument to be tracked.

$$\mathbf{J_I} = \begin{pmatrix} 0 & 0 & -\dfrac{f\sigma_0}{\sigma^2} & 0 \\ \dfrac{1}{f + \dfrac{u^2}{f}} & 0 & 0 & 0 \\ 0 & \dfrac{1}{f + \dfrac{v^2}{f}} & 0 & 0 \\ 0 & 0 & 0 & 1 \end{pmatrix}, \tag{27}$$

with f the focal length of the camera's lens. This hybrid visual and force feedback scheme is shown in Fig. 12. The PC (600 Mhz) is used for image processing, force sampling and to control the robot at a sampling rate of 50 Hz. For the practical experiments, we apply a triangle signal on the feature coordinate u varying between -100 and 100 pixels at a frequency of 0.05 Hz (see Fig. 13). According to the geometrical configuration of the camera and instrument it corresponds to a displacement of ± 2 cm of the instrument. Therefore, 5 pixels in the image correspond to 1 mm in space. The other visual features are kept equal to zero. The results displayed on Fig. 14 present the error on the visual feature u and the force $\mathbf{f}_x$
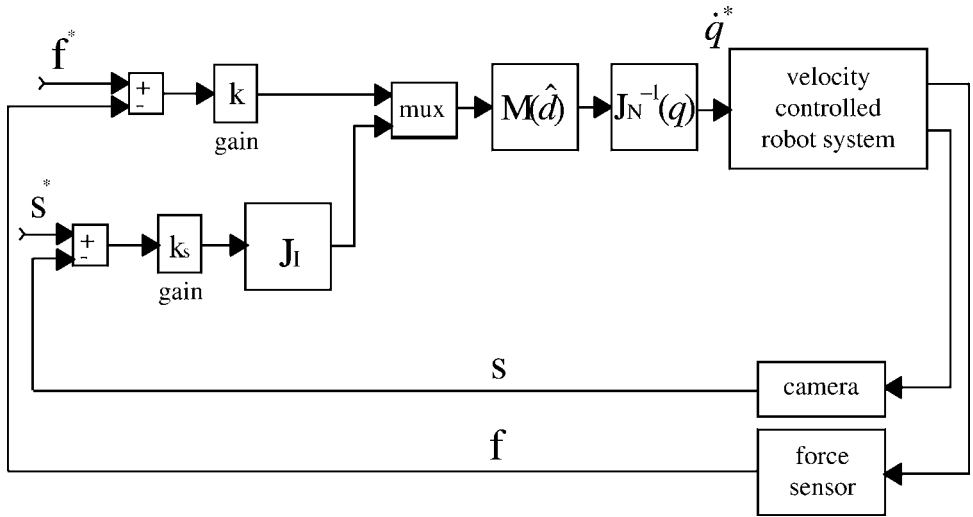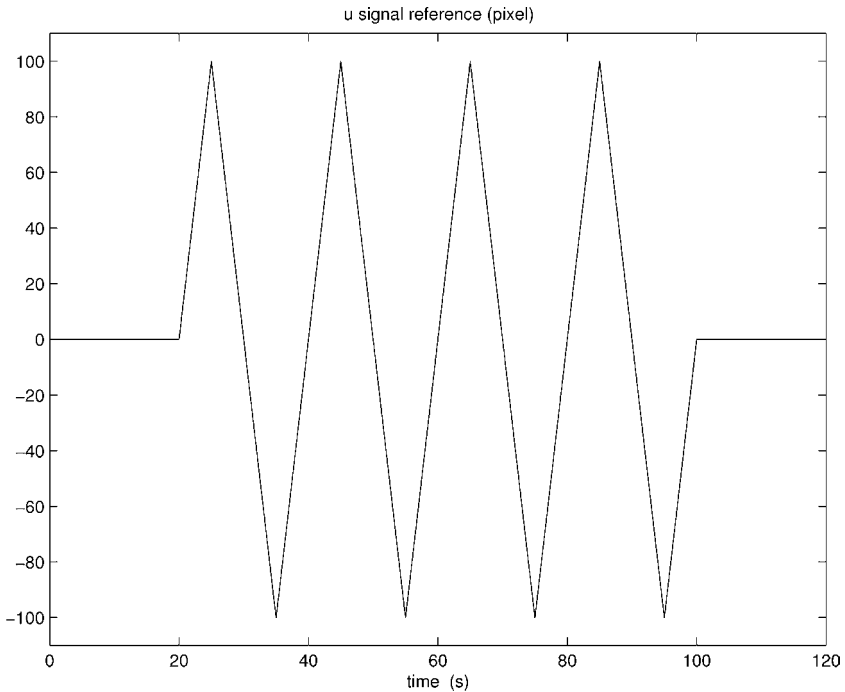
Figure 12. Hybrid visual and force control.

Figure 13. Signal reference of visual feature u.

measured when the estimated parameter $\widehat{d}$ is kept constant, $\widehat{d} = d_0$. In the second configuration, $\widehat{d} = 0.3$ m and $d = 0.1$ m the maximum visual error on the feature tracking is $|u_{\text{error}}| \simeq 40$ pixels with a maximum force $|\mathbf{f}_x| \simeq 5$ N. One can see that
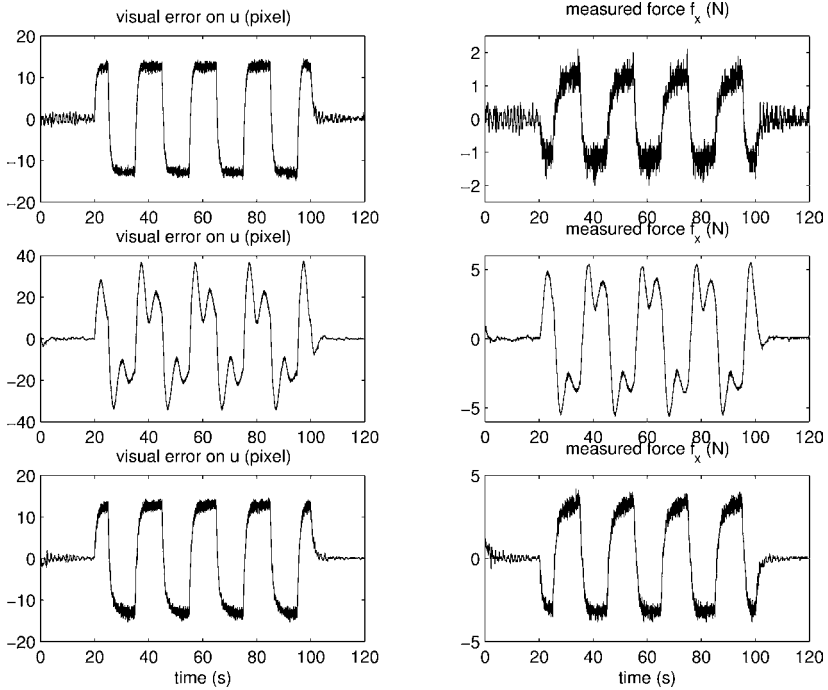
Figure 14. Error on visual feature u and force $\mathbf{f}_x$ with estimated parameter $\widehat{d} = d_0$ constant. First row: $d_0 = 0.15$ m and $d = 0.2$ m. Second row: $d_0 = 0.3$ m and $d = 0.1$ m. Third row: $d_0 = 0.02$ m and $d = 0.2$ m.

the error signal of the camera motion is smooth compared to the force vibration. This is due to the integral behavior of the closed loop system and the choice of a low control gain $\mathbf{k}_s$ which guarantees the stability of the visual servoing by reducing the bandwidth of the system. Figures 15 and 16 show, respectively, the same experiments when $\widehat{d}$ is estimated with the gradient algorithm estimator of Section 4 and with the robust least-squares estimator of Section 5. For these two experiments, when the initial configuration is $\widehat{d} = d_0 = 0.3$ m with $d = 0.1$ m, the maximum visual error obtained on the feature tracking is $|u_{\text{error}}| \simeq 20$ pixels. Once the convergence of the estimate of d is obtained, the force $|\mathbf{f}_x|$ converges closely to 1 N and the control performance is similar for the two on-line estimation approaches. So we can see that with on-line estimation of d, it is possible to keep forces low as well as perform visual tracking in a laparoscopic environment. The gradient algorithm estimator exhibits a rather slower convergence of the depth estimation as compared to direct least-squares estimation. However, the estimated signal $\widehat{d}$ is smoother and more accurate ($\simeq 7$ mm). This is due to the dynamics of the gradient law that acts on $\widehat{d}$, whereas the least-squares algorithm gives instantaneously the estimation of d with a poor accuracy ($\simeq 5$ cm).
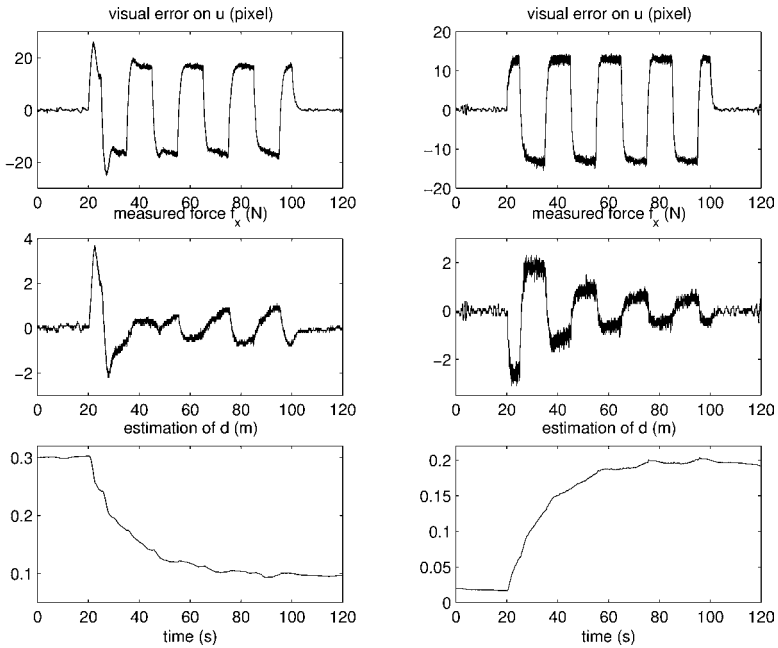
Figure 15. Error on visual feature u and force $\mathbf{f}_x$ with gradient algorithm estimation of d. Left column: $d_0 = 0.3$ m and $d = 0.1$ m. Right column: $d_0 = 0.02$ m and $d = 0.2$ m.
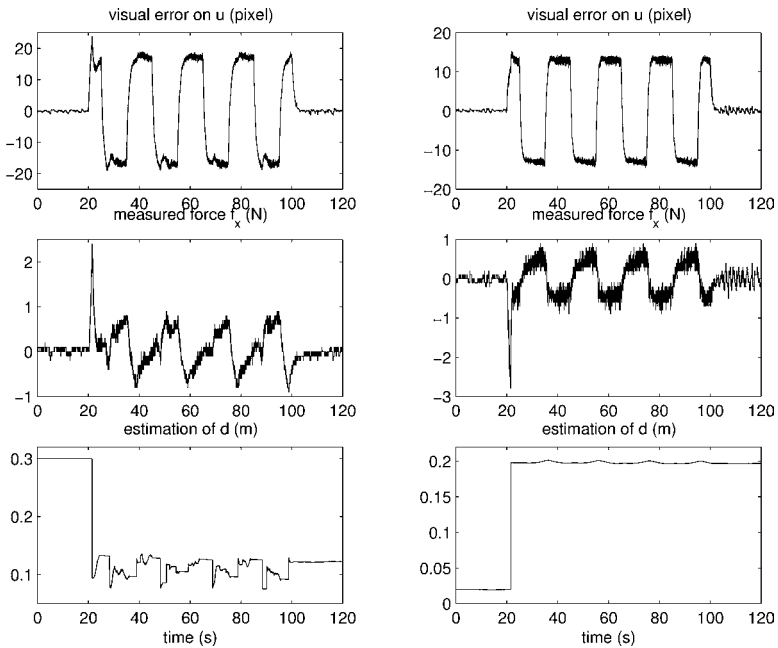

Figure 16. Error on visual feature u and force $\mathbf{f}_x$ with robust least-squares identification of d. Left column: $d_0 = 0.3$ m and $d = 0.1$ m. Right column: $d_0 = 0.02$ m and $d = 0.2$ m.

7. CONCLUSION

In this paper, we have proposed to use a 6-d.o.f. actuated robot to hold surgical instruments for laparoscopic manipulation. Force-feedback control strategies have been proposed to solve the trocar kinematic constraint, involving the on-line estimation of the environment geometry. They have been experimentally validated. Furthemore, an experiment where an instrument is tracked by the endoscope has been performed.

REFERENCES

1. G. Guthart and J. K. Salisbury, The intuitive telesurgery system: overview and applications, in: *Proc. of ICRA 2000*, San Francisco, CA (2000).
2. A. Madhani, G. Niemeyer and J. K. Salisbury, The Black Falcon: a teleoperated surgical instrument for minimally invasive surgery, in: *Proc. IEEE/RSJ Int. Conf. on Intelligent Robots and Systems*, Victoria, BC (1998).
3. http://www.computermotion.com
4. A. Krupa, J. Gangloff, C. Doignon, M. de Mathelin, G. Morel, J. Leroy, L. Soler and J. Marescaux, Autonomous 3-D positioning of surgical instruments in robotized laparoscopic surgery using visual servoing, *IEEE Trans. Robotics Automat.* **19**, 842–853 (2003).
5. A. Krupa, G. Morel and M. de Mathelin, Achieving high precision laparoscopic manipulation through adaptive force control, in: *Proc. IEEE Int. Conf. on Robotics and Automation*, Washington, DC, pp. 1864–1869 (2002).
6. L. Villani, C. Canudas de Wit and B. Borglioato, An exponentially stable adaptove control for force and position tracking of robot manipulators, *IEEE Trans. Automatic Control* **44**, 798–802 (1999).
7. L. Villani, C. Natale, B. Siciliano and C. Canudas de Wit, An experimental study of adaptive force/position control algorithms for an industrial robot, *IEEE Trans. Control Syst. Technol.* **8**, 777–786 (2000).
8. M. de Mathelin and R. Lozano, Robust adaptive identification of slowly time-varying parameters with bounded disturbances, *Automatica* **35**, 1291–1305 (1999).
9. G.-Q. Wei, K. Arbter and G. Hirzinger, Real-time visual servoing for laparoscopic surgery, *IEEE Engng Med. Biol.* **16**, 40–45 (1997).
10. A. Casals, J. Amat, D. Prats and E. Laporte, Vision guided robotic system for laparoscopic surgery, in: *Proc. IFAC Int. Congr. on Advanced Robotics*, Barcelona (1995).
11. Y-F. Wang, D. R. Uecker and Y. Wang, A new framework for vision-enabled and robotically assisted minimally invasive surgery, *Comp. Med. Imaging Graphics* **22**, 429–437 (1998).
12. F. Chaumette, P. Rives and B. Espiau, Classification and realization of the different vision-based tasks, in: *Visual Servoing*, K. Hashimoto (Ed.), pp. 199–228. World Scientific Press, Singapore (1993).
13. S. Sastry and M. Bodson, *Adaptive Control: Stability, Convergence, and Robustness*. Prentice-Hall. Englewood Cliffs, NJ (1989).

APPENDIX

DEFINITION (Norms). If x is a possibly time-varying vector, then:

- $\| x(t) \|$ is the Euclidean norm of x at time t
- $\| x \|_2 = [\int_0^\infty \| x(\tau) \|^2 \, d\tau]^{1/2}$
- $\| x \|_\infty = \sup_{0 \leqslant t} \| x(t) \|$

and $x \in L_2$ when $\| x \|_2$ exists, $x \in L_\infty$ when $\| x \|_\infty$ exists. If A is a possibly time-varying matrix, then $\| A \|$, $\| A \|_2$ and $\| A \|_\infty$ will be the induced norms of A.

Proof of Lemma 1.

1. Let us define the following Lyapunov-like function:

$$V(t) = \frac{1}{2}e_p^2 = \frac{1}{2}\left(d - \widehat{d}\right)^2 \geqslant 0. \tag{A1}$$

Using (13) and (14), one gets:

$$\dot{V}(t) = e_p \left(k_1\left(\dot{\mathbf{f}}_x + gk\mathbf{f}_x\right)\frac{\omega_y^*}{\epsilon + \omega_x^{*2} + \omega_y^{*2}} - k_1\left(\dot{\mathbf{f}}_y + gk\mathbf{f}_y\right)\frac{\omega_x^*}{\epsilon + \omega_x^{*2} + \omega_y^{*2}} \right)$$

$$= -k_1 g \left(\frac{\omega_x^{*2} + \omega_y^{*2}}{\epsilon + \omega_x^{*2} + \omega_y^{*2}} \right) e_p^2. \tag{A2}$$

Thus $\dot{V}(t) \leqslant 0$ and $V \in L_\infty$. Therefore, $\widehat{d}$ and $\dot{\widehat{d}} \in L_\infty$.

2. From (A2), it follows that:

$$\int_0^\infty \frac{\omega_x^{*2} + \omega_y^{*2}}{\epsilon + \omega_x^{*2} + \omega_y^{*2}} e_p^2 \, dt = \frac{1}{k_1 g}(V(0) - V_\infty) \tag{A3}$$

therefore,

$$\sqrt{\frac{\omega_x^{*2} + \omega_y^{*2}}{\epsilon + \omega_x^{*2} + \omega_y^{*2}}} e_p \in L_2.$$

3. Since $V \geqslant 0$ and $\dot{V} \leqslant 0$, it follows that $V(t)$ is a monotically decreasing function bounded below by zero. Consequently, $\lim_{t \to \infty} V(t) = V_\infty$ and $\lim_{t \to \infty} e_p(t) = e_{p\infty}$.

4. From (A2):

$$\dot{V}(t) = -2k_1 g \left(\frac{\omega_x^{*2} + \omega_y^{*2}}{\epsilon + \omega_x^{*2} + \omega_y^{*2}} \right) V(t). \tag{A4}$$

Therefore, using Theorem 2.5.1 in Ref. [13], if

$$\sqrt{\frac{\omega_x^{*2} + \omega_y^{*2}}{\epsilon + \omega_x^{*2} + \omega_y^{*2}}}$$

is persistently exciting, then $\lim_{t \to \infty} V(t) = 0$ exponentially, and $\lim_{t \to \infty} e_p = 0$ exponentially.

Proof of Lemma 2.

1. Let us define the following Lyapunov-like function:

$$V(t) = \frac{1}{2} [d - \widehat{d} \quad g - \widehat{g}] \begin{bmatrix} g & 0 \\ 0 & 1 \end{bmatrix} \begin{bmatrix} d - \widehat{d} \\ g - \widehat{g} \end{bmatrix}$$

$$= \frac{e_p^{\mathrm{T}} A e_p}{2} \geqslant 0 \tag{A5}$$

with $A = \begin{bmatrix} g & 0 \\ 0 & 1 \end{bmatrix}$. Using (13) and (17), one gets:

$$\dot{V}(t) = e_p^{\mathrm{T}} A \dot{e}_p = -k_1 e_p^{\mathrm{T}} \mathbf{Q} e_p \tag{A6}$$

with:

$$\mathbf{Q} = \begin{pmatrix} \dfrac{g^2}{\rho^2}(\omega_x^{*2} + \omega_y^{*2}) & \dfrac{gk}{\rho^2}(\mathbf{f}_x \omega_y^* - \mathbf{f}_y \omega_x^*) \\ gk(\mathbf{f}_x \omega_y^* - \mathbf{f}_y \omega_x^*) & k^2(\mathbf{f}_x^2 + \mathbf{f}_y^2) \end{pmatrix}$$

with $\rho(t) = \sqrt{\epsilon + \omega_x^{*2}(t) + \omega_y^{*2}(t)}$.

From Sylvester's theorem, the quadratic function $\dot{V}(t)$ is semi-definite negative, if and only if, the upper left submatrices of $\mathbf{Q}$ have non-negative determinants. Since:

$$\mathbf{Q}_{11} = \frac{g^2}{\rho^2}(\omega_x^{*2} + \omega_y^{*2}) \geqslant 0$$

$$\det(\mathbf{Q}) = \frac{g^2 k}{\rho^2}(\mathbf{f}_x \omega_x^* + \mathbf{f}_y \omega_y^*)^2 \geqslant 0$$

therefore, $\mathbf{Q} \geqslant 0$, $\dot{V}(t) \leqslant 0$ and $V \in L_\infty$. It follows that $e_p \in L_\infty$ and, using (17), $\widehat{d}$ and $\widehat{g} \in L_\infty$.

2. From (A6), we have:

$$\dot{e}_p = -k_1 \mathbf{Q} e_p \tag{A7}$$

with $\mathbf{Q} \geqslant 0$, therefore if $\mathbf{Q}^{1/2}$ is persistently exciting, i.e.

$$\exists \eta > 0 \; \exists T \text{ s.t. } \frac{1}{T} \int_{t_0}^{t_0+T} \mathbf{Q} \, \mathrm{d}t > \eta I > 0, \quad \forall t_0 \geqslant 0$$

using Theorem 2.5.1 in Ref. [13], then $\lim_{t \to \infty} \dot{e}_p = 0$, exponentially.

ABOUT THE AUTHORS

Alexandre Krupa was born in 1976 in Strasbourg, France. He received the MS (DEA) and PhD degrees in Control Science and Signal Processing from the National Polytechnic Institute of Lorraine, Nancy, France in 1999 and 2003, respectively. He is currently working in robotics in the Laboratoire des Sciences de l'Image, de l'Informatique et de la Télédétection (LSIIT) at the University of Strasbourg I, Illkirch, France. His research interests include medical robotics, visual servoing of robotic manipulators, computer vision and micro-robotics.

Guillaume Morel obtained his PhD at the University of Paris 6 in 1994. He has been successively a Postdoctoral Research Assistant at the Department of Mechanical Engineering of the Massachusetts Institute of Technology (1995–1996) and an Associate Professor at the University of Strasbourg, France (1997–2000). After a year in the industrial world, as a Research Scientist for the French Company of Electricity (EDF, 2000–2001) he has been back the academic world since September 2001, at the Laboratoire de Robotique de Paris, France. His research has concerned the sensor-based control of robots, with a particular focus on force-feedback control and visual servoing. Application of these techniques for medical robotics is now the main area of his reserach.

Michel de Mathelin received the Electrical Engineering degree from Louvain University, Louvain-La-Neuve, Belgium, in 1987. He completed his MS and PhD degrees in Electrical and Computer Engineering at Carnegie Mellon University, Pittsburgh, PA in 1988 and 1993, respectively. He was a Research Scientist in the Electrical Engineering Department of the Polytechnic School of the Royal Military Academy, Brussels, Belgium, during the 1991–1992 academic year. In 1993, he became Maître de Conférences at the Université Louis Pasteur (Strasbourg I University), France. Since 1999, he has been Professor at the Ecole Nationale Supérieure de Physique de Strasbourg (ENSPS). He is a Fellow of the Belgian American Educational Foundation. His research interests include adaptive and robust control, visual servoing, and medical robotics.